PHYSICAL REVIEW A **102**, 051102(R) (2020)

Rapid Communications

Attosecond XUV probing of vibronic quantum superpositions in Br_2^+

Yuki Kobayashi,[1,*] Daniel M. Neumark,[1,2,†] and Stephen R. Leone[1,2,3,‡]
[1]*Department of Chemistry, University of California, Berkeley, California 94720, USA*
[2]*Chemical Sciences Division, Lawrence Berkeley National Laboratory, Berkeley, California 94720, USA*
[3]*Department of Physics, University of California, Berkeley, California 94720, USA*

(Received 27 June 2020; accepted 20 October 2020; published 13 November 2020)

Ultrafast laser excitation can create coherent superpositions of electronic states in molecules and trigger ultrafast flow of electron density on a few femtosecond timescale. While recent attosecond experiments have addressed real-time observation of these primary photochemical processes, the underlying roles of simultaneous nuclear motions and how they modify and disturb the valence electronic motion remain uncertain. Here, we investigate coherent electronic-vibrational dynamics induced among multiple vibronic levels of ionic bromine (Br_2^+), including both spin-orbit ($X^2\Pi_{3/2,g} - X^2\Pi_{1/2,g}$) and valence ($A^2\Pi_{3/2,u} - {}^4\Sigma_{3/2,u}$) electronic superpositions, using attosecond transient absorption spectroscopy. Decay, revival, and apparent frequency shifts of electronic coherences are measured via characteristic quantum beats on the Br-3*d* core-level absorption signals. Quantum-mechanical simulations attribute the observed electronic decoherence to broadened phase distributions of nuclear wave packets on anharmonic potentials. Molecular vibronic structure is further revealed to be imprinted as discrete progressions in electronic beat frequencies. These results provide a future basis to interpret complex charge-migration dynamics in polyatomic systems.

DOI: 10.1103/PhysRevA.102.051102

The most elementary step of photochemical reactions is the ultrafast response of valence electrons that occur faster than the subsequent rearrangements of molecular geometry [1,2]. These pure electronic dynamics are described by coherent superpositions of two or more electronic states, in which the interference between electronic wave functions gives rise to oscillations of total electron density, while few-electron-volt energy spacings of valence electronic levels dictate that the timescales of electronic motions can be as short as few- to sub-femtosecond. The advent of high-harmonic-generation-based attosecond x-ray sources has enabled experimental access to coherent electronic dynamics at their natural timescales [3–5]. Early attosecond experiments demonstrated that strong-field ionization can prepare coherent superpositions of valence spin-orbit states in rare-gas atoms [6,7]. Coherent electronic motion occurring through chemical bonds, a process known as charge migration, has been reported in a few molecular systems and is attracting wide attention [8,9].

Despite recent success in the characterization of electronic coherences, the roles of simultaneous nuclear motions remain elusive. In a model case where the nuclear motions are frozen, coherent electronic dynamics continue indefinitely at a fixed period. In a real system with moving nuclei, however, molecular vibrations, dissociation, and potential crossings occur on femtosecond timescales, perturbing the phase and overlap relations between the electronic states [2]. Furthermore, the nuclear degrees of freedom in molecules add complexity to the energy landscapes of electronic dynamics. Instantaneous energy spacings of electronic states change in time as molecular vibrations and dissociation occur, which translate to apparent frequency shifts of coherent electronic motions. The characteristics of bound or dissociative potential surfaces determine the frequency spectra of electronic quantum beats, in an analogous way to discrete vibrational progressions or continuous spectral bands commonly found in optical absorption or photoelectron spectra [10].

Many of the previous attosecond experiments were on atomic systems [6,7,11,12], and studies on molecular electronic-vibrational dynamics are rare. A few recent experiments reported observations of electronic-rotational coherences in small molecules, and they provided first examples of electronic decoherence caused by nuclear motions [13,14]. However, no significant effects of electronic-vibrational coherences, which are crucial to the charge-migration dynamics, were reported as the observations were limited to electronic coherences in spin-orbit doublet states [11,13–17]. In optical-domain experiments, electronic superpositions were reported for the Fenna-Matthews-Olsen photosynthetic complex [18], which generated considerable discussion concerning the role of electronic versus vibrational coherences in large molecules. In attosecond charge-migration studies, the role of vibrational motions has been considered in the context of decoherence, and theoretical predictions await experimental verifications [19–24]. Revealing the role of nuclear motions in regulating and perturbing electronic coherences is fundamental to attochemistry [25] and ultimately to designing ultrafast laser control of photochemical dynamics [26,27].

Here, we present an attosecond transient absorption study on coherent electronic-vibrational dynamics of ionic

---

[*] ykoba@berkeley.edu
[†] dneumark@berkeley.edu
[‡] srl@berkeley.edu

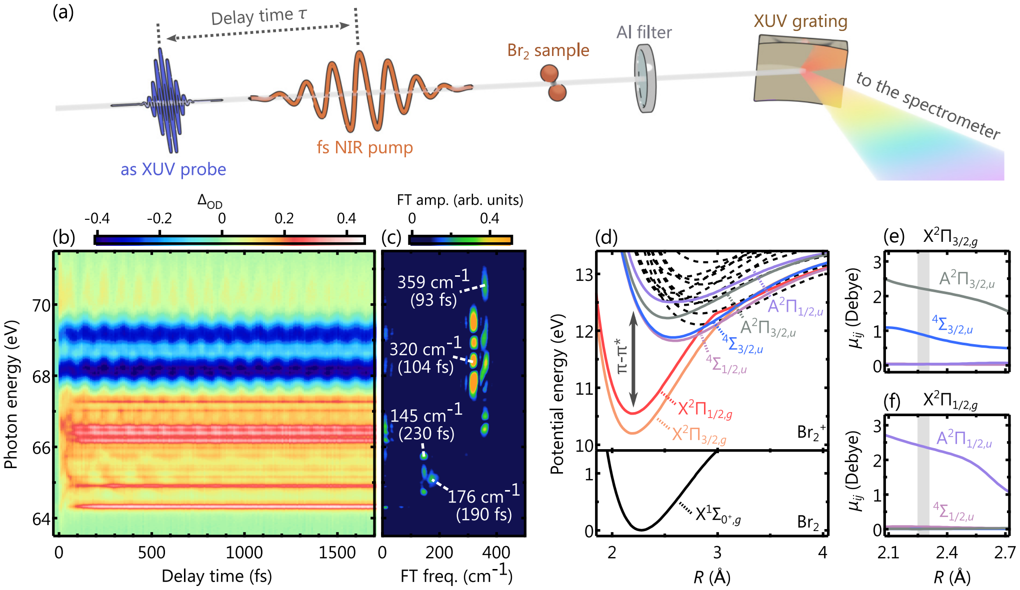

FIG. 1. Outline of the experiments, long-delay measurements, and electronic structure of bromine. (a) Illustration of the attosecond transient absorption setup. (b) Long-delay transient absorption spectra of bromine. Vibrational dynamics induced among multiple bound ionic states are clearly resolved. (c) Fourier-transform (FT) analysis of the transient absorption spectra. The FT frequencies and the corresponding vibrational periods are denoted. (d) *Ab initio* potential energy curves of bromine. (e), (f) Transition dipole moments from the (e) $X\,^2\Pi_{3/2,g}$ and (f) $X\,^2\Pi_{1/2,g}$ states to the excited electronic states. The gray shades show the Franck-Condon region of the neutral bromine.

molecular bromine ($Br_2{}^+$). This species has several bound electronic states in the valence levels [28–30], and thus offers an ideal platform to study vibronic superpositions. The results highlight critical roles of molecular vibrations in causing decay and revival of electronic coherence as well as regulating frequency spectra of valence-electronic superpositions.

Figure 1(a) shows the schematic of the experiment. A few-cycle near-infrared (NIR) pulse (<4 fs, $\sim 5 \times 10^{14}$ W/cm^2) induces strong-field ionization and excitation of bromine, launching coherent superpositions among its ionic electronic states. A subsequent attosecond extreme-ultraviolet (XUV) pulse (<200 as) arriving after a delay time τ probes the coherent dynamics via Br-3d core-level absorption at photon energies of $\sim$65 eV. Pump-on and pump-off XUV spectra are collected at each delay time, and the absorption spectrum is defined by the differential optical density, $\Delta_{\mathrm{OD}}(\omega, t) = -\ln[I_{\mathrm{on}}(\omega, t)/I_{\mathrm{off}}(\omega, t)]$. Transitions from core orbitals, whose energies and shapes remain nearly unperturbed throughout the reaction coordinates, serve as sensitive reporters of valence dynamics [31]. Basic experimental conditions required to characterize electronic coherences are as follows: (i) the temporal duration of the pump pulse is shorter than the timescales of electronic coherences and (ii) the probe pulse has a sufficiently broad bandwidth to promote the valence-state populations to a common final state. The few-cycle NIR pump, attosecond XUV probe configuration of this experiment satisfies these requirements, and electronic coherences manifest as characteristic quantum beats in the transient absorption signals [32].

Figure 1(b) shows the transient absorption spectra recorded from -30 fs to 1700 fs in 10-fs intervals. The vibrational dynamics are characterized in this long-delay measurement, which allows tentative state assignments to be made. Figure 1(c) shows the Fourier transform analysis of the transient absorption spectra, and Fig. 1(d) shows *ab initio* potential energy curves of bromine highlighting the relevant electronic states.

The higher frequency features at 320 cm^{-1} and 359 cm^{-1} match the harmonic frequency of the neutral $X\,^1\Sigma_{0^+,g}$ state (323.3 cm^{-1}) and those of the ionic $X\,^2\Pi_{3/2,g}$ and $X\,^2\Pi_{1/2,g}$ states (364.9 cm^{-1} and 361.2 cm^{-1}), respectively [28,29]. These ground-state vibrational features have already been characterized in a previous study with 40-fs NIR excitation [33]. The lower vibrational frequencies at 176 cm^{-1} and 145 cm^{-1} are newly observed in this experiment, and they can be assigned to loosely bound ionic excited states, $A\,^2\Pi_u$ and $^4\Sigma_u$ [Fig. 1(d)]. The experimentally known harmonic frequencies are 205.0 cm^{-1}, 160.8 cm^{-1}, 200.6 cm^{-1}, and 197.8 cm^{-1} for the $^2\Pi_{3/2,u}$, $^2\Pi_{1/2,u}$, $^4\Sigma_{3/2,u}$, and $^4\Sigma_{1/2,u}$ states, respectively [30]. The deviations between the measured and reference harmonic frequencies implicate a vibrational anharmonicity and a significant manifold of higher vibrational states excited among these electronic states.

Electronic coherences are characterized in short-delay measurements recorded from -17 fs to 466 fs in 1.5-fs intervals [Fig. 2(a)]. Note that coherences between the different g/u symmetry states, i.e., $X\,^2\Pi_g$ and $A\,^2\Pi_u/^4\Sigma_u$, cannot be detected in the present probing scheme because the $g \leftrightarrow u$ selection rule prohibits the different g/u states to reach a common final state. The main focus is on two spectral regions marked as X (66.7–67.0 eV) and A/Σ (64.5–64.9 eV) [Fig. 2(a)], wherein the faster (359 cm^{-1}) and slower

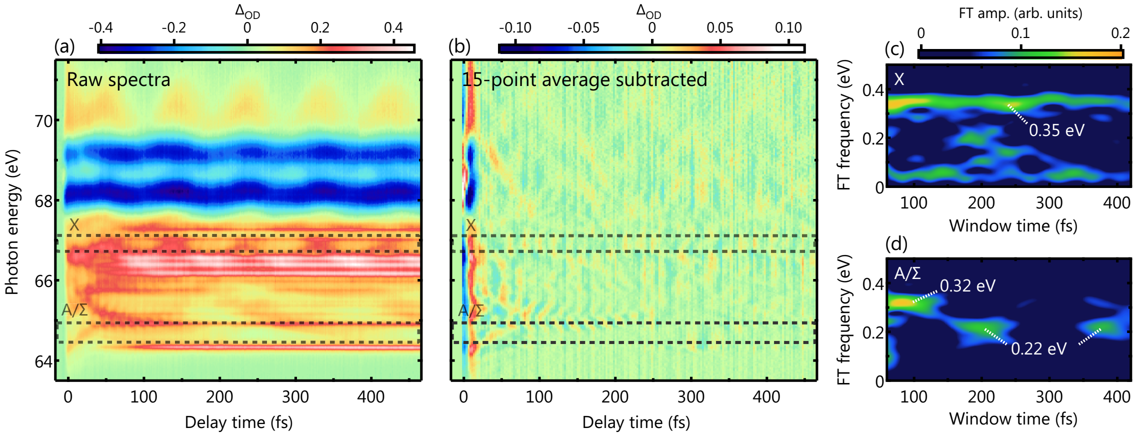

FIG. 2. Short-time measurements for electronic coherences. (a) Transient absorption spectra of bromine recorded from −30 fs to 1700 fs in 1.5-fs intervals. Two spectral regions X (66.7–67.0 eV) and A/Σ (64.5–64.9 eV) are marked by dashed boxes. (a) Transient absorption spectra after subtracting a 15-point data average. (c), (d) Window Fourier-transformation analysis of the transient absorption spectra for (c) region X and (d) region A/Σ. In region X, a constant beat frequency of 0.35 eV is observed, representing electronic coherence in the $X\,^2\Pi_g$ states. In region A/Σ, dramatic variations of the beat frequency and amplitude are observed. These results are indicative of important roles of vibrational motions to maneuver electronic quantum beats.

(145 cm^{-1} and 176 cm^{-1}) vibrational signals are observed, respectively. Instantaneous beat frequencies are analyzed first by subtracting a 15-point data average to remove slowly varying components [Fig. 2(b)] and then taking a window Fourier transformation (FT) in regions X and A/Σ with an 85-fs super-Gaussian function [Figs. 2(c) and 2(d)]. The results around zero delay time are not discussed because of the strong zero-frequency background originating from the sharp rise of the ionic signals (see Supplemental Material Fig. S1 for the full spectrogram [34]).

In region X, a constant beat frequency of 0.35 eV (11.9-fs periodicity) is observed [Fig. 2(c)]. This value matches the spin-orbit splitting in the $X\,^2\Pi_g$ states (0.350 eV) [29], and it can be assigned to electronic coherence between the $X\,^2\Pi_{3/2,g}$ and $X\,^2\Pi_{1/2,g}$ states. This result reaffirms that strong-field ionization driven by a few-cycle NIR pulse can create coherent superpositions of the spin-orbit doublet states in the ground-state ions, as already demonstrated for several atomic and molecular systems [6,7,11,15,17].

The electronic quantum beats in region A/Σ exhibit an entirely different behavior [Fig. 2(d)]. A quantum beat of 0.32 eV is observed around 100 fs and it decays in time. A new beat feature at 0.22 eV emerges transiently around 200 fs, and the same frequency component revives around 400 fs. The apparent frequency shifts as well as the decay and revival of the quantum beats are particularly important as they are indicative of the unique role of the vibrational motions underlying electronic decoherence and recoherence.

To investigate the origin of the observed quantum beats, coherent wave-packet dynamics of bromine are simulated by numerically solving the time-dependent Schrödinger equation. The states included in the simulations are $X\,^2\Pi_{3/2,g}$ and $X\,^2\Pi_{1/2,g}$ for region X, and $A\,^2\Pi_{3/2,u}$ and $^4\Sigma_{3/2,u}$ for region A/Σ. The strong π-π^* transitions [Figs. 1(d)–1(f)] are considered as an excitation route to prepare the electronic quantum beats observed in region A/Σ (see Supplemental Material for the details [34]). The initial wave packets are created by vertical projection of the neutral ground-state wave function. The nuclear wave packets on two different electronic states, $\psi_i(R,t)$ and $\psi_j(R,t)$, are characterized by the coherence C_{ij} and spatial overlap S_{ij} that are defined as [21]

$$C_{ij}(t) = \mathrm{Re}\left[\int \psi_i^*(R,t)\psi_j(R,t)dR\right], \tag{1}$$

$$S_{ij}(t) = \int |\psi_i^*(R,t)\psi_j(R,t)|dR. \tag{2}$$

The real term is taken for the coherence instead of its absolute value in order to visualize the actual beats. This coherence can be associated with the observed quantum beats assuming that the XUV absorption strengths are largely invariant within the region of the vibrational motions. Comparison between C_{ij} and S_{ij} helps identify whether decoherence is caused by the loss of spatial overlap ($S_{ij} \approx |C_{ij}|$), or by dephasing ($S_{ij} > |C_{ij}|$) [21,35]. The effect of molecular rotations, which is known to cause slow variation in the x-ray absorption amplitude on picosecond timescales [17,36,37], is not considered in this study.

The nuclear wave-packet motions on the $X\,^2\Pi_{3/2,g}$ and $X\,^2\Pi_{1/2,g}$ potentials are shown in Figs. 3(a) and 3(b), respectively. The energy spacing between the two potentials is relatively flat in the vicinity of the equilibrium distance [Fig. 3(c)], as it mostly originates from the spin-orbit coupling in the π^* orbital. The $X\,^2\Pi_{3/2,g}$ and $X\,^2\Pi_{1/2,g}$ states thus exhibit identical vibrational motions, and the spatial overlap and coherence between the nuclear wave packets are perfectly maintained throughout the simulated time range [Fig. 3(d)]. The window-FT analysis is performed on the simulated coherence, and the result is shown in Fig. 3(e). The simulation reproduces the observed quantum beat at 0.35 eV, providing clear confirmation of the signal assignment.

The nuclear wave-packet motions on the $A\,^2\Pi_{3/2,u}$ and $^4\Sigma_{3/2,u}$ potentials are shown in Figs. 3(f) and 3(g),

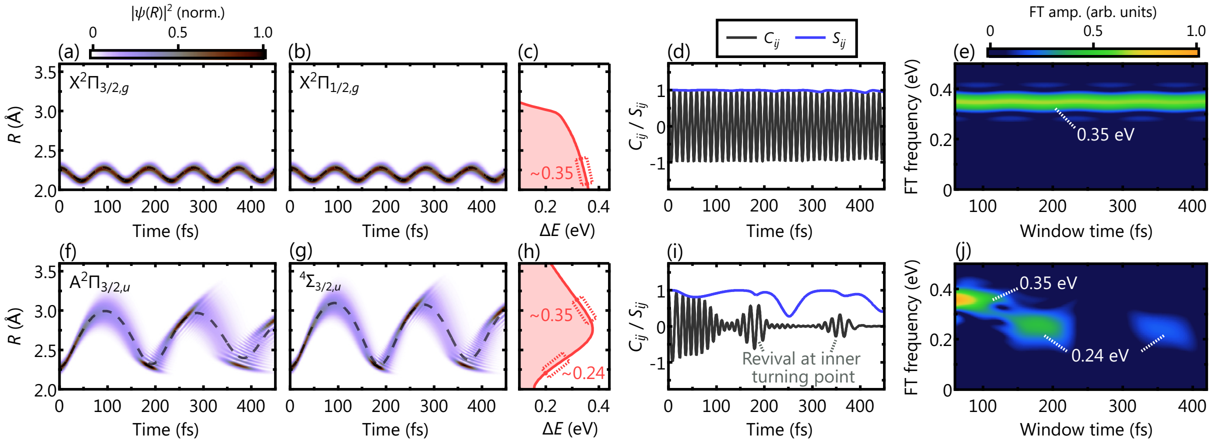

FIG. 3. Wave-packet simulation of the electronic quantum beats. (a), (b) A false-color plot for the simulated probability distributions of the nuclear wave packets on the (a) $X\,^2\Pi_{3/2,g}$ and (b) $X\,^2\Pi_{1/2,g}$ states. Black dashed curves show the center of amplitude of the wave packets. (c) Energy spacing (ΔE) between the $X\,^2\Pi_{3/2,g}$ and $X\,^2\Pi_{1/2,g}$ states as a function of the internuclear distance. The dashed box highlights the energy spacing around the region of the vibrational motion. (d) Spatial overlap (S_{ij}, blue curve) and electronic coherence (C_{ij}, gray curve) between the nuclear wave packets on the $X\,^2\Pi_{3/2,g}$ and $X\,^2\Pi_{1/2,g}$ states. (e) Window Fourier-transform analysis of the calculated electronic coherence in (d). The constant 0.35 eV component well reproduces the experimental results. (f),(g) Simulated probability distributions of the nuclear wave packets on the (f) $A\,^2\Pi_{3/2,u}$ and (g) $^4\Sigma_{3/2,u}$ states. (h) Energy spacing between the $A\,^2\Pi_{3/2,u}$ and $^4\Sigma_{3/2,u}$ states as a function of the internuclear distance. The dashed boxes highlight the energy spacings around the inner and outer turning points of the vibrational motions. (i) Spatial overlap (blue curve) and electronic coherence (gray curve) between the nuclear wave packets on the $A\,^2\Pi_{3/2,u}$ and $^4\Sigma_{3/2,u}$ states. (j) Window Fourier-transform analysis of the calculated electronic coherence in (i). The experimentally observed frequency shifting and beat revival are reproduced.

respectively. The wave packets sweep across the two loosely bound potentials, with the center of amplitude (dashed curves) reaching $R \approx 3.0$ Å. The wave packets return to the inner turning point at 193 fs and 186 fs for the $A\,^2\Pi_{3/2,u}$ and $^4\Sigma_{3/2,u}$ states, respectively, and these calculated periods agree with the experimentally observed period of 190 fs [Fig. 1(c)]. The coherence and spatial overlap exhibit dramatic variation as the wave packets evolve on the highly anharmonic potentials [Fig. 3(i)]. The window-FT analysis is shown in Fig. 3(j), and the simulated results successfully reproduce the experimental electronic quantum beats including the frequency shifting and the beat revival [Fig. 2(d)]. The two beat frequencies, 0.35 eV and 0.24 eV [Fig. 3(j)], approximately correspond to the energy spacings of the $A\,^2\Pi_{3/2,u}$ and $^4\Sigma_{3/2,u}$ potentials at the outer turning points and inner turning points, respectively [Fig. 3(h)]. The correspondence between the instantaneous beat frequencies and the inner and outer energy spacings is further verified in a cosine-function fitting analysis (Fig. S2 [34]).

More insights into the coherence dynamics are obtained by inspecting the wave-packet motions and comparing S_{ij} and C_{ij} [Figs. 3(f)–3(i)]. The wave packets maintain a high degree of coherence after the excitation until they reach the outer turning points at ∼100 fs [Fig. 3(i)], as they have a large spatial overlap and a well-defined phase relation. As the wave packets return from the outer turning points, the spatial overlap remains large but the coherence starts to exhibit a gradual decrease [Fig. 3(i)]. This is because the wave packets are broadened at the outer turning points by the significant anharmonicity of the excited potentials, and the developed phase distribution leads to a temporary decoherence. When the wave packets return to the inner turning points at ∼190 fs [Figs. 3(f) and 3(g)], they are localized at the same initial position of $R = 2.3$ Å, a well-defined phase relation is recovered, and the electronic coherence revives [Fig. 3(i)]. The recovered electronic coherence does not last long, because the spatial overlap sharply decreases when the wave packets leave the inner turning points. The revival of electronic coherence occurs when the wave packets are localized again at the inner turning point (∼380 fs), while the accrued effects of dephasing between the nuclear wave packets result in a smaller beat amplitude (∼50% decrease).

So far, the electronic-vibrational dynamics have been viewed as a pair of nuclear wave packets moving on two electronic potentials, and the observed instantaneous beat frequencies are associated with the energy spacings that vary as a function of the internuclear distance. Alternatively, each wave packet can be viewed as a superposition of multiple vibrational eigenfunctions, and this picture brings to light that electronic quantum beats should consist of a finite number of frequency components that strictly correspond to discrete energy spacings of vibronic levels.

The first step for analyzing the vibronic structure is to decompose the coherence term into pairs of vibrational eigenfunctions,

$$C_{ij}(t) = \mathrm{Re}\left[\sum_{v,v'} a_v^*(t) b_{v'}(t) \int \phi_v^*(R)\varphi_{v'}(R)dR\right] \tag{3}$$

$$= \mathrm{Re}\left[\sum_{v,v'} p_{v,v'} S_{v,v'} e^{i\theta_{v,v'}} e^{-i\Delta\omega_{v,v'}t}\right]. \tag{4}$$

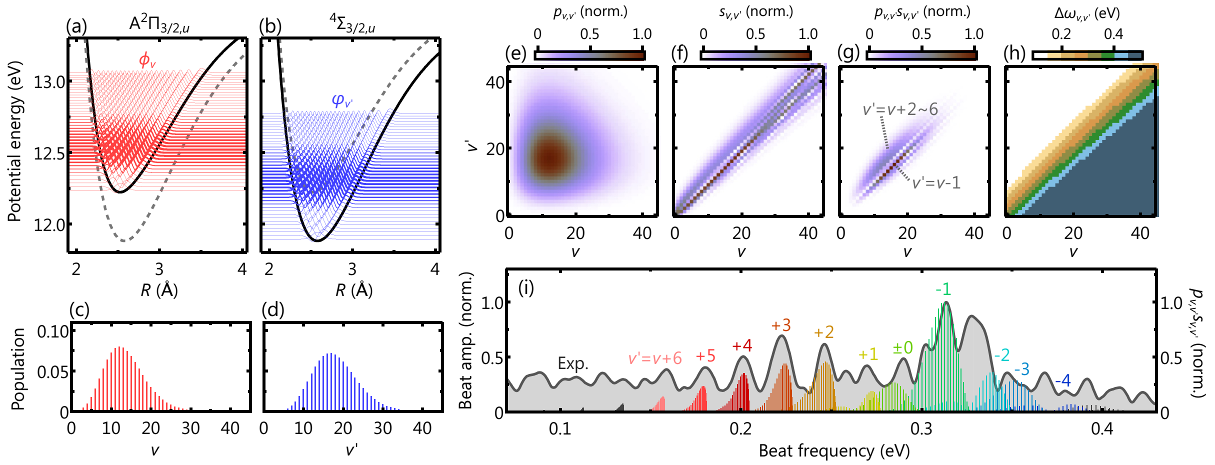

FIG. 4. Vibronic-structure analysis of the electronic quantum beats. (a),(b) Vibrational eigenfunctions of the (a) $A\,^2\Pi_{3/2,u}$ and (b) $^4\Sigma_{3/2,u}$ states. The vibronic levels $v = 0$–50 are plotted with their thickness representing the relative populations. The solid and dashed lines show the potential energy curves of the two states. (c),(d) Population distributions calculated from the vertical projection of the neutral ground-state wave packet onto the ionic potentials. (e)–(h) Summary of the vibronic state analysis, i.e., (e) cross population term $p_{v,v'}$, (f) cross overlap term $s_{v,v'}$, (g) total products $p_{v,v'}s_{v,v'}$, and (h) the energy spacing $\Delta\omega_{v,v'}$. (i) Comparison between the experimental beat frequency (gray area) and the calculated weight of the v-v' pairs. Different coloring is used to distinguish the main $v = v + n$ series ($n = -4 \sim +6$).

ϕ_v ($\varphi_{v'}$) is the vth (v'th) vibrational eigenfunction of the ith (jth) electronic state and a_v ($b_{v'}$) is its complex coefficient. In the present case, the state indexes i and j refer to the $A\,^2\Pi_{3/2,u}$ and $^4\Sigma_{3/2,u}$ states, respectively. Note that the amplitudes of a_v and $b_{v'}$ are constant as the molecule has only one vibrational mode. The vibrational eigenfunctions as well as the calculated population distributions assuming the vertical projection of the neutral wave function onto the $A\,^2\Pi_{3/2,u}$ and $^4\Sigma_{3/2,u}$ states are shown in Figs. 4(a)–4(d). The weight of each v-v' vibronic pair is given by a cross population $p_{v,v'} = |a_v^*(0)b_{v'}(0)|$ and a cross overlap $S_{v,v'} = |\int \phi_v^*(R)\varphi_{v'}(R)dR|$. The phase evolves at a constant rate of $\Delta\omega_{v,v'}$. The initial phase information is stored in $\theta_{v,v'}$, which is unimportant for the current analysis.

Among the numerous v-v' pairs populated by the strong-field excitation, the overlap term factors out only those with $v \approx v'$ because of the approximate orthogonality between the vibrational eigenfunctions [Fig. 4(f)]. The product weight terms $p_{v,v'}s_{v,v'}$ are shown in Fig. 4(g). The $v' = v - 1$ series makes the largest contribution, and the $v' = v + (2$–$6)$ series yield additional contributions. The energy spacings of the v-v' pairs are shown in Fig. 4(h). Within the same $v' = v + n$ series, the energy spacings vary only by a few meV corresponding to the difference in the harmonic frequencies of the two potentials, whereas the neighboring n and $n + 1$ series are separated by ~0.023 eV (or ~180 cm^{-1}), which is equal to the experimentally measured vibrational frequency for the ionic excited states [Fig. 1(c)].

The calculated weights of the v-v' pairs are compared to a frequency spectrum of the experimental quantum beats in region A/Σ [Fig. 4(i)]. In the plot, the calculated energy spacings are shifted by −0.04 eV to take into account an overestimate in the adiabatic excitation energies (see Table S1 [34]). A good match is seen between the strongest peak at 0.32 eV and the calculated $v' = v - 1$ series, and also between the sequence of the peaks from 0.15 eV to 0.25 eV and the calculated $v' = v + (2$–$6)$ series. Only the $v' = v + n$ series are resolved in the present experiments, but an extended scan of ~10 ps duration, according to simulations, will ultimately reveal individual v-v' pairs (see Fig. S3 [34]). In the conventional Franck-Condon analysis for optical absorption or photoelectron spectra, spatial overlap is taken between vibrational eigenfunctions of the initial and final states of an optical excitation, and a vibrational progression represents simultaneous excitation of electronic and vibrational states in molecules. Here, the spatial overlap is taken between the nuclear wave packets on two electronic potentials, and the progression signifies the molecular vibronic structure translated as discretized beat frequencies of the coherent electronic motions.

This work establishes a prominent role of vibrational motions in maneuvering the observed electronic quantum beats in molecules. In the anharmonic potentials of bromine, the broadening of the nuclear wave packets transiently leads to decoherence, and the revival of the electronic quantum beats occur when the wave packets are localized at the inner turning points. Potential anharmonicity is a ubiquitous effect and will be a critical factor for designing long-lived electronic coherences in large molecules. It is further demonstrated that coherent electronic motion in molecules are subject to additional quantization by the vibrational dynamics. It bears mentioning that the effects of molecular rotations and intramolecular vibrational redistribution (IVR) are not considered in this study, as they are slower (picosecond) dynamics for rotation compared to the vibronic coherence and nonexistent in the case of IVR. In principle, rovibrational structure can be observed in electronic quantum-beat spectra by taking extended delay-time measurements, and IVR may cause irreversible decoherence in polyatomic molecules by coupling different vibrational modes. Investigation of these effects is a subject for future experiments. Knowing the temporal behavior and precise frequencies of coherent electronic motions is fundamental for triggering and capturing charge migration, and this study paves the way toward subfemtosecond laser engineering of chemical reactivity.

This material is based upon a work supported by the National Science Foundation Grants No. CHE-1660417 and No. CHE-1951317 (Y.K., S.R.L.) and the US Army Research Office Grants No. W911NF-14-1-0383 (Y.K., D.M.N., S.R.L.) and No. W911NF-20-1-0127 (D.M.N.). Y.K. also acknowledges financial support by the Funai Overseas Scholarship.

[1] S. R. Leone, C. W. McCurdy, J. Burgdörfer, L. S. Cederbaum, Z. Chang, N. Dudovich, J. Feist, C. H. Greene, M. Ivanov, R. Kienberger, U. Keller, M. F. Kling, Z.-H. Loh, T. Pfeifer, A. N. Pfeiffer, R. Santra, K. Schafer, A. Stolow, U. Thumm, and M. J. J. Vrakking, Nat. Photonics **8**, 162 (2014).

[2] H. J. Wörner, C. A. Arrell, N. Banerji, A. Cannizzo, M. Chergui, A. K. Das, P. Hamm, U. Keller, P. M. Kraus, E. Liberatore, P. Lopez-Tarifa, M. Lucchini, M. Meuwly, C. Milne, J.-E. Moser, U. Rothlisberger, G. Smolentsev, J. Teuscher, J. A. van Bokhoven, and O. Wenger, Struct. Dyn. **4**, 061508 (2017).

[3] P. B. Corkum and F. Krausz, Nat. Phys. **3**, 381 (2007).

[4] F. Krausz and M. Ivanov, Rev. Mod. Phys. **81**, 163 (2009).

[5] K. Ramasesha, S. R. Leone, and D. M. Neumark, Annu. Rev. Phys. Chem. **67**, 41 (2016).

[6] E. Goulielmakis, Z.-H. Loh, A. Wirth, R. Santra, N. Rohringer, V. S. Yakovlev, S. Zherebtsov, T. Pfeifer, A. M. Azzeer, M. F. Kling, S. R. Leone, and F. Krausz, Nature (London) **466**, 739 (2010).

[7] A. Wirth, M. T. Hassan, I. Grguraš, J. Gagnon, A. Moulet, T. T. Luu, S. Pabst, R. Santra, Z. A. Alahmed, A. M. Azzeer, V. S. Yakovlev, V. Pervak, F. Krausz, and E. Goulielmakis, Science **334**, 195 (2011).

[8] F. Calegari, D. Ayuso, A. Trabattoni, L. Belshaw, S. De Camillis, S. Anumula, F. Frassetto, L. Poletto, A. Palacios, P. Decleva, J. B. Greenwood, F. Martín, and M. Nisoli, Science **346**, 336 (2014).

[9] P. M. Kraus, B. Mignolet, D. Baykusheva, A. Rupenyan, L. Horný, E. F. Penka, G. Grassi, O. I. Tolstikhin, J. Schneider, F. Jensen, L. B. Madsen, A. D. Bandrauk, F. Remacle, and H. J. Wörner, Science **350**, 790 (2015).

[10] G. Herzberg, *Molecular Spectra and Molecular Structure. I. Spectra of Diatomic Molecules* (D. Van Nostrand Company, Inc., New York, 1950).

[11] A. Fleischer, H. J. Wörner, L. Arissian, L. R. Liu, M. Meckel, A. Rippert, R. Dörner, D. M. Villeneuve, P. B. Corkum, and A. Staudte, Phys. Rev. Lett. **107**, 113003 (2011).

[12] Y. Kobayashi, M. Reduzzi, K. F. Chang, H. Timmers, D. M. Neumark, and S. R. Leone, Phys. Rev. Lett. **120**, 233201 (2018).

[13] P. M. Kraus, S. B. Zhang, A. Gijsbertsen, R. R. Lucchese, N. Rohringer, and H. J. Wörner, Phys. Rev. Lett. **111**, 243005 (2013).

[14] A. Rudenko, V. Makhija, A. Vajdi, T. Ergler, M. Schürholz, R. K. Kushawaha, J. Ullrich, R. Moshammer, and V. Kumarappan, Faraday Discuss. **194**, 463 (2016).

[15] H. Timmers, X. Zhu, Z. Li, Y. Kobayashi, M. Sabbar, M. Hollstein, M. Reduzzi, T. J. Martínez, D. M. Neumark, and S. R. Leone, Nat. Commun. **10**, 3133 (2019).

[16] T. Ando, E. Lötstedt, A. Iwasaki, H. Li, Y. Fu, S. Wang, H. Xu, and K. Yamanouchi, Phys. Rev. Lett. **123**, 203201 (2019).

[17] Y. Kobayashi, K. F. Chang, S. M. Poullain, V. Scutelnic, T. Zeng, D. M. Neumark, and S. R. Leone, Phys. Rev. A **101**, 063414 (2020).

[18] G. S. Engel, T. R. Calhoun, E. L. Read, T.-K. Ahn, T. Mančal, Y.-C. Cheng, R. E. Blankenship, and G. R. Fleming, Nature (London) **446**, 782 (2007).

[19] G. J. Halász, A. Perveaux, B. Lasorne, M. A. Robb, F. Gatti, and A. Vibók, Phys. Rev. A **88**, 023425 (2013).

[20] V. Despré, A. Marciniak, V. Loriot, M. C. E. Galbraith, A. Rouzée, M. J. J. Vrakking, F. Lépine, and A. I. Kuleff, J. Phys. Chem. Lett. **6**, 426 (2015).

[21] M. Vacher, M. J. Bearpark, M. A. Robb, and J. P. Malhado, Phys. Rev. Lett. **118**, 083001 (2017).

[22] C. Arnold, O. Vendrell, and R. Santra, Phys. Rev. A **95**, 033425 (2017).

[23] V. Despré, N. V. Golubev, and A. I. Kuleff, Phys. Rev. Lett. **121**, 203002 (2018).

[24] D. Jia, J. Manz, and Y. Yang, J. Phys. Chem. Lett. **10**, 4273 (2019).

[25] F. Calegari, G. Sansone, S. Stagira, C. Vozzi, and M. Nisoli, J. Phys. B: At., Mol. Opt. Phys. **49**, 062001 (2016).

[26] F. Remacle and R. D. Levine, Proc. Natl. Acad. Sci. **103**, 6793 (2006).

[27] F. Lépine, M. Y. Ivanov, and M. J. J. Vrakking, Nat. Photonics **8**, 195 (2014).

[28] J. Coxon, J. Mol. Spectrosc. **37**, 39 (1971).

[29] T. Harris, J. Eland, and R. Tuckett, J. Mol. Spectrosc. **98**, 269 (1983).

[30] H. Liang, Z. Zhou, Z. Hua, Y. Zhao, S. Feng, Y. Chen, and D. Zhao, J. Phys. Chem. A **123**, 4609 (2019).

[31] R. Geneaux, H. B. J. Marroux, A. Guggenmos, D. M. Neumark, and S. R. Leone, Philos. Trans. R. Soc. London A **377**, 20170463 (2019).

[32] R. Santra, V. S. Yakovlev, T. Pfeifer, and Z.-H. Loh, Phys. Rev. A **83**, 033405 (2011).

[33] E. R. Hosler and S. R. Leone, Phys. Rev. A **88**, 023420 (2013).

[34] See Supplemental Material at http://link.aps.org/supplemental/10.1103/PhysRevA.102.051102 for details of the methods and additional analyses, which includes Refs. [38–50].

[35] G. A. Fiete and E. J. Heller, Phys. Rev. A **68**, 022112 (2003).

[36] N. Saito, H. Sannohe, N. Ishii, T. Kanai, N. Kosugi, Y. Wu, A. Chew, S. Han, Z. Chang, and J. Itatani, Optica **6**, 1542 (2019).

[37] P. Peng, C. Marceau, and D. M. Villeneuve, Nat. Rev. Phys. **1**, 144 (2019).

[38] H. Timmers, Y. Kobayashi, K. F. Chang, M. Reduzzi, D. M. Neumark, and S. R. Leone, Opt. Lett. **42**, 811 (2017).

[39] M. W. Schmidt, K. K. Baldridge, J. A. Boatz, S. T. Elbert, M. S. Gordon, J. H. Jensen, S. Koseki, N. Matsunaga, K. A. Nguyen, S. Su, T. L. Windus, M. Dupuis, and J. A. Montgomery, J. Comput. Chem. **14**, 1347 (1993).

[40] T. Zeng, J. Chem. Phys. **146**, 144103 (2017).

[41] Y. Kobayashi, T. Zeng, D. M. Neumark, and S. R. Leone, Struct. Dyn. **6**, 014101 (2019).

[42] T. Zeng, D. G. Fedorov, and M. Klobukowski, J. Chem. Phys. **131**, 124109 (2009).

[43] T. Zeng, D. G. Fedorov, and M. Klobukowski, J. Chem. Phys. **132**, 074102 (2010).

[44] T. Zeng, D. G. Fedorov, and M. Klobukowski, J. Chem. Phys. **133**, 114107 (2010).

[45] T. Zeng, D. G. Fedorov, and M. Klobukowski, J. Chem. Phys. **134**, 024108 (2011).

[46] D. T. Colbert and W. H. Miller, J. Chem. Phys. **96**, 1982 (1992).

[47] C. Leforestier, R. Bisseling, C. Cerjan, M. Feit, R. Friesner, A. Guldberg, A. Hammerich, G. Jolicard, W. Karrlein, H.-D. Meyer, N. Lipkin, O. Roncero, and R. Kosloff, J. Comput. Phys. **94**, 59 (1991).

[48] O. P. J. Vieuxmaire, M. G. D. Nix, J. A. J. Fitzpatrick, M. Beckert, R. N. Dixon, and M. N. R. Ashfold, Phys. Chem. Chem. Phys. **6**, 543 (2004).

[49] K. Balasubramanian, Chem. Phys. **119**, 41 (1988).

[50] E. R. Hosler, Ultrafast strong-field vibrational dynamics studied by femtosecond extreme-ultraviolet transient absorption spectroscopy, Ph.D. thesis, University of California, Berkeley, 2013.